In-place molecular preservation of cellulose in 5,000-year-old archaeological textiles

Corentin Reynaud[a], Mathieu Thoury[a], Alexandre Dazzi[b], Gaël Latour[c,d], Mario Scheel[e], Jiayi Li[a], Ariane Thomas[f], Christophe Moulhérat[g], Aurore Didier[h], and Loïc Bertrand[a,e,i,1]

[a]Université Paris-Saclay, CNRS, Ministère de la Culture, UVSQ, Institut photonique d'analyse non-destructive européen des matériaux anciens, 91192, Saint-Aubin, France; [b]Université Paris-Saclay, CNRS, Institut de Chimie Physique, 91405, Orsay, France; [c]Laboratoire d'Optique et Biosciences, École Polytechnique, CNRS, INSERM, Institut Polytechnique de Paris, 91128 Palaiseau, France; [d]Université Paris-Saclay, 91190, Saint-Aubin, France; [e]Synchrotron SOLEIL, 91192 Gif-sur-Yvette, France; [f]Musée du Louvre, 75008 Paris, France; [g]Musée du Quai Branly–Jacques Chirac, 75007 Paris, France; [h]Archéologies et Sciences de l'Antiquité, CNRS, UMR 7041, Univ Paris-Nanterre, Univ. Paris I Panthéon-Sorbonne, Ministère de la Culture, 92000 Nanterre, France; [i]Université Paris-Saclay, ENS Paris-Saclay, CNRS, Photophysique et Photochimie Supramoléculaires et Macromoléculaires, 91190 Gif-sur-Yvette, France

Edited by Matthew J. Collins, University of Copenhagen, Copenhagen, Denmark, and accepted by Editorial Board Member Lia Addadi June 17, 2020 (received for review March 23, 2020)

The understanding of fossilization mechanisms at the nanoscale remains extremely challenging despite its fundamental interest and its implications for paleontology, archaeology, geoscience, and environmental and material sciences. The mineralization mechanism by which cellulosic, keratinous, and silk tissues fossilize in the vicinity of archaeological metal artifacts offers the most exquisite preservation through a mechanism unexplored on the nanoscale. It is at the center of the vast majority of ancient textiles preserved under nonextreme conditions, known through extremely valuable fragments. Here we show the reconstruction of the nanoscale mechanism leading to the preservation of an exceptional collection of ancient cellulosic textiles recovered in the ancient Near East (4,000 to 5,000 years ago). We demonstrate that even the most mineralized fibers, which contain inorganic compounds throughout their histology, enclose preserved cellulosic remains in place. We evidence a process that combines the three steps of water transport of biocidal metal cations and soil solutes, degradation and loss of crystallinity of cellulosic polysaccharides, and silicification.

cultural heritage | fossilization | cellulosic textiles | nanoimaging | synchrotron

Fossils retain a morphological imprint of original tissues, thus providing valuable information from a past geological age (1–3). Organic residues present in some fossils can be found in an "exquisite" state of chemical preservation (4–6). In the fossil record, cellulose shows limited resilience over long periods of time. It has been found in sufficient quantities to be identified as a biomolecule in only a limited number of fossil plants, apart from when engaged in lignin–cellulose complexes, such as in petrified woods (7–9). The initial steps after burial are critical to lead to exceptional preservation (10) as, in most sedimentary contexts, degradation of cellulosic remains will occur in a few weeks only (11). Experiments to reproduce in vitro the fate of organic cellulosic systems have provided valuable evidence, although it remains particularly difficult to define conditions that model these behaviors in experiments of realistic duration. Particular attention should be paid to the study of century- and millennia-old samples, such as cellulosic textiles, that have undergone modifications on time scales that cannot be reproduced in the laboratory (12, 13). Apart from environmental contexts of exceptional dryness, wetness, or coldness, preserved archaeological cellulosic textiles are primarily found in the close vicinity of metal artifacts as "mineralized" systems (11, 14–17). For archaeology, they are the precious direct evidence of textile production thousands of years ago (18, 19). However, it has remained particularly difficult to understand these "mineralization" processes, the study of which requires coherent corpuses in terms of contexts, type of material, and age, in a highly constrained archaeological record (11, 20).

The study of an exceptional set of ancient cellulosic textiles recovered in sites from the ancient Near East led us to propose a physico-chemical mechanism at the origin of their exceptional preservation at the nanoscale. The coupling of nanoresolved photonic techniques in the infrared, the visible, and the X-ray domains provides access to their structure and composition. Our results show the intricate relationship between the mineralization and silicification mechanisms at micrometric and nanometric scales. The experimental evidence gathered has led us to a consistent interpretation suggesting that mineralization resulted from successive steps of water transport of biocidal metal cations and solutes from the environment, macromolecular degradation and loss of crystallinity of cellulosic material, and a final step of condensation of siliceous compounds.

Significance

We report on the oldest archaeological textiles studied in detail for the mechanisms leading to their exceptional preservation, issued from archaeological excavations in the Ancient East and from collections of the Louvre Museum. We have studied these fossilized hybrid organic–mineral systems at high spatial resolution, from nano- to microscale, using a combination of nanoinfrared near-field spectroscopy, second harmonic generation microscopy, semiquantitative synchrotron X-ray microtomography, and electron microscopy. We establish a physicochemical pathway leading to their exceptional preservation. We show the joint involvement of the two main long-standing paradigms of mineralization and silicification in the process. We consistently identified "pockets of molecular preservation" with a demonstration of the in-place preservation of cellulose microfibrillar assemblies from SHG microscopy.

Author contributions: M.T. and L.B. conceived the original project; L.B. coordinated the research; C.R. organized all experiments; A. Dazzi, G.L., and M.S. developed the experimental setups and implemented the experiments; A.T., C.M., and A. Didier provided access to the samples and interpretation of the archaeological contexts; C.R., M.T., A. Dazzi, G.L., M.S., J.L., and L.B. took part in the experiments; C.R. processed the data with M.T. and L.B.; C.R., M.T., J.L., and L.B. provided the interpretation; C.R. and L.B. prepared the figures; and C.R. and L.B. wrote the paper.

The authors declare no competing interest.

This article is a PNAS Direct Submission. M.J.C. is a guest editor invited by the Editorial Board.

Data deposition: All data for this paper are available in the Zenodo repository: https://doi.org/10.5281/zenodo.3712368.

[1]To whom correspondence may be addressed. Email: loic.bertrand@universite-paris-saclay.fr.

This article contains supporting information online at https://www.pnas.org/lookup/suppl/doi:10.1073/pnas.2004139117/-/DCSupplemental.

First published August 3, 2020.

Inorganic Phases Identification at the Nanoscale

We studied archaeological cellulosic fibers found exceptionally preserved morphologically in the close vicinity of copper-based objects, from three fragmentary archaeological textiles (third to second millenium BCE, Gonur-Depe, present-day Turkmenistan; third millenium BCE, Nausharo, present-day Pakistan; and second millenium BCE, Tello, present-day Iraq; *SI Appendix*, Fig. S1). For a more detailed presentation of the material, please refer to *Materials and Methods* and to the sample corpus description in *SI Appendix*, Text S1. Synchrotron X-ray microtomography (μ-CT) (21) confirms the increasing degree of mineralization of the samples according to the sequence Gonur-Depe, Nausharo, Tello, in coherence with optical microscopy observations (Fig. 1 *A* and *B* and *SI Appendix*, Fig. S1). While Gonur-Depe fibers appear exceptionally well preserved with an organic core surrounded by thin inorganic layers, Nausharo fibers are characterized by a weaker contrast between the inorganic crust and the fibers, indicating that they have been impregnated with mineral-rich solutions. Plant fibers consist of organic cell walls (primary and secondary walls) surrounding a lumen. Tello fibers are "positively mineralized" (the shape of the fibers was preserved while their polymeric matrix has been replaced by corrosion compounds) (19) with the presence of inorganic compounds in all cell walls, leading to their distinct blue-green hue, and strongly absorb X-rays (*SI Appendix*, Fig. S1).

Our semiquantitative μ-CT protocol allows estimating the local attenuation coefficient, $\mu_E(X)$, in each voxel X of the reconstructed volumes (*Materials and Methods* and *SI Appendix*, Text S1). Numerical adjustment of the μ-CT attenuation histograms by sets of Gaussian functions led to the identification of five distinct phases in our samples (Fig. 1*D*). Each phase is characterized by an average linear attenuation coefficient $\langle \mu_E^i \rangle$ which we compared to computed values from compounds associated with the long-term corrosion of copper artifacts in soils (*SI Appendix*, Table S2). A very low attenuation phase dominates the less-mineralized sample from Gonur-Depe ($\langle \mu_E \rangle = 49\ \mathrm{cm}^{-1}$), typically attributable to organic compounds. A phase of intermediate attenuation (116 to 120 cm^{-1}) is identified in both Gonur-Depe and Nausharo samples. Three additional unexpected inorganic phases with higher attenuation are observed. A phase at ca. 180 cm^{-1} is detected in the Gonur-Depe and Nausharo samples, a phase at ca. 250 cm^{-1} is present in all archaeological samples, and a high-attenuation phase centered at ca. 350 cm^{-1} is identified only in the sample from Tello (Fig. 1*D* and *SI Appendix*, Table S1). The spatial segmentation of these distinct phases in the volumes was carried out by

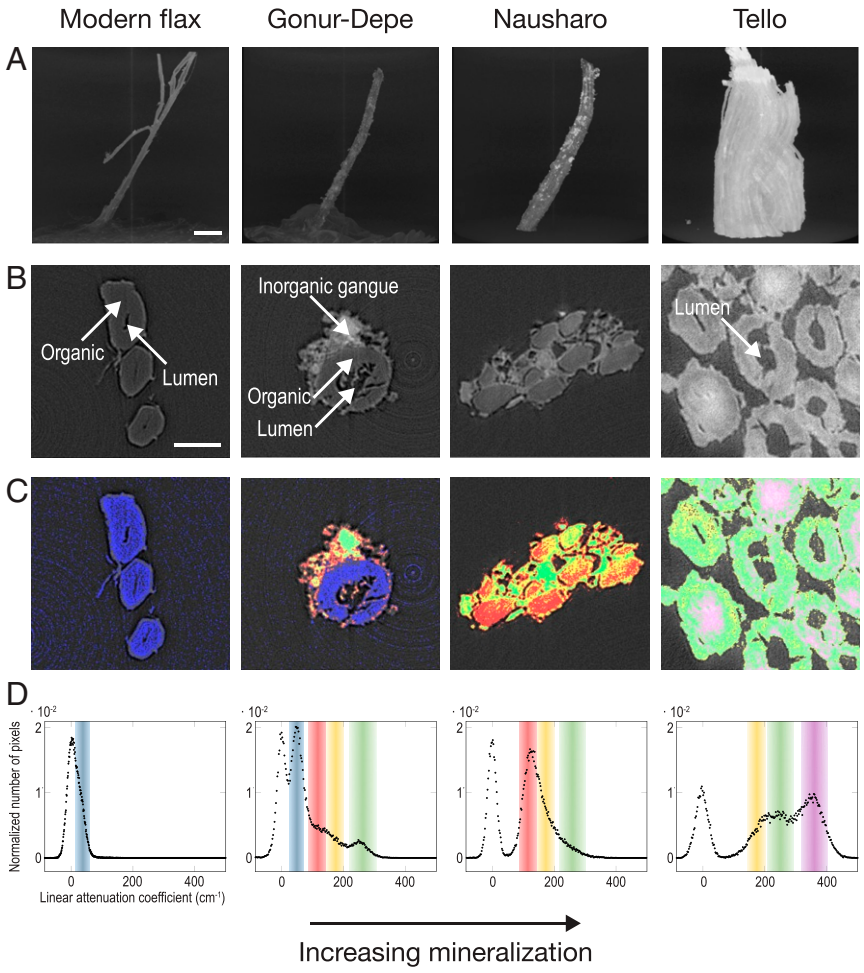

Fig. 1. Submicrometric morphological and chemical description of fibers from Gonur-Depe, Nausharo, and Tello from semiquantitative synchrotron X-ray microtomography. (*A* and *B*) The 3D reconstructions (*A*) and virtual sections (*B*) associated with the three archaeological samples and the modern flax reference (46). (*C*) Images obtained by segmentation of the virtual sections showing the distribution of the main constituent phases using the color coding in *D*. (Scale bars: 100 μm in *A* and 20 μm in *B* and *C*.) (*D*) Histograms of the distribution of linear attenuation coefficients collected on zones from each virtual section (blue, organic phase; red, phase composed of soluble calcium, silicon, and copper compounds; yellow, green, and purple, copper silicates; see text for interpretation and *SI Appendix*, Text S1 for details).

highlighting the pixels associated with each Gaussian distribution (Fig. 1*C* and *SI Appendix*, Text S2 and Fig. S8). In the Gonur-Depe sample, this digital processing confirms the presence of an organic core surrounded by a ca. 5-μm thin crust of corrosion and soil products of a complex composition based on energy-dispersive X-ray (EDX) spectroscopy detection of elements such as copper, sodium, chlorine, silicon, magnesium, and phosphorus on the surface of the fiber (*SI Appendix*, Fig. S9). In the Nausharo sample, μ-CT shows the absence of any organic core and scanning electron microscopy (SEM)-EDX analysis of the fiber surface shows the presence of copper, silicon, aluminum, and chlorine as the main chemical elements (*SI Appendix*, Fig. S9). In the Tello fibers, segmentation shows that the three inorganic phases of higher attenuation complement each other by filling the entire cell region and the lumen of several fibers. Surface SEM-EDX analysis reveals the almost exclusive presence of copper and silicon (*SI Appendix*, Fig. S9).

Exceptional Preservation of Organic Residues Even in the Most Ancient Fibers at the Nanoscale

Dehydrated modern flax fibers contain by mass ca. 70% cellulose, 20% hemicelluloses, and other compounds in smaller amounts (in particular lignin, pectins, and waxes) (22). In all three archaeological samples, including in the most chemically transformed fibers from the Nausharo and Tello sites, we have consistently identified cellulosic Fourier transform infrared (FTIR) signatures, suggesting that mineralization did not lead to the "total replacement" of the original organic material by inorganic compounds (Fig. 2). They appear almost exclusively cellulosic, as shown by the surprisingly well-preserved "signature" domain in the FTIR spectra, in terms of both spectral bands and stoichiometry (Fig. 2 and *SI Appendix*, Table S4). These organic residues, 4,000 to 5,000 years old, are the oldest relic traces of organic matter reported so far in archaeological textiles. We consistently observed the disappearance of the characteristic hemicelluloses absorption bands at 1,731 and 1,255 cm^{-1}, attributed to C=O bond elongation, and methoxy C–O bond elongation modes, respectively (*SI Appendix*, Table S4). As amorphous polymers, hemicelluloses are particularly prone to deacetylation and depolymerization by hydrolysis and are likely to have degraded in subunits of a sufficiently low degree of polymerization to be solubilized in water and leached out by environmental waters (23). We collected absolute μ-FTIR absorbance spectra (corrected for the sample thickness measured by atomic force microscopy; *SI Appendix*, Text S1) to compare semiquantitatively the differential preservation of organic compounds between the fibers. The more the fibers are mineralized, the less their organic residues are preserved, as shown by the decrease in the intensity of the cluster of absorption bands around 2,900 cm^{-1} attributed to the stretching modes of the alkyl bonds of cellulose (C–H, CH_2; Fig. 2), which is attributed to a significant cleavage of the organic macromolecules by hydrolysis and oxidation. The presence of hydrolyzed cellulosic residues in the fibers results in a low intensity of the absorption bands at 1,161, 1,058, and 1,035 cm^{-1}, associated with vibrations of the β-1,4-glycosidic bridges C–O bonds, in comparison to modern flax (Fig. 2 and *SI Appendix*, Table S4). The hydrolysis of cellulose has led to its partial depolymerization by breaking β-1,4-glycosidic bridges, which induces the formation of subunits that are poorly soluble in water at neutral pH and may therefore remain in place in the material (24). Oxidation of cellulose hydroxyl groups can occur in an aerobic environment and leads to the formation of byproducts containing carbonyl and/or carboxyl groups. Ancient fibers (as untreated, native, reference fibers) contain adsorbed water characterized by an absorption band at 1,635 cm^{-1} in μ-FTIR, corresponding to the deformation vibration modes of H–O–H bonds. The fibers from Tello show signs of oxidation of hydroxyl groups from cellulosic residues as shown by the increase in intensity of the absorption band at ca. 1,625 cm^{-1} in μ-FTIR, which is attributed to an increase in carboxylates (1,610 cm^{-1}) and not adsorbed water (1,635 cm^{-1}), as shown by the concomitant slight displacement of this massif toward lower wavenumbers, compared to the other spectra (25) (Fig. 2).

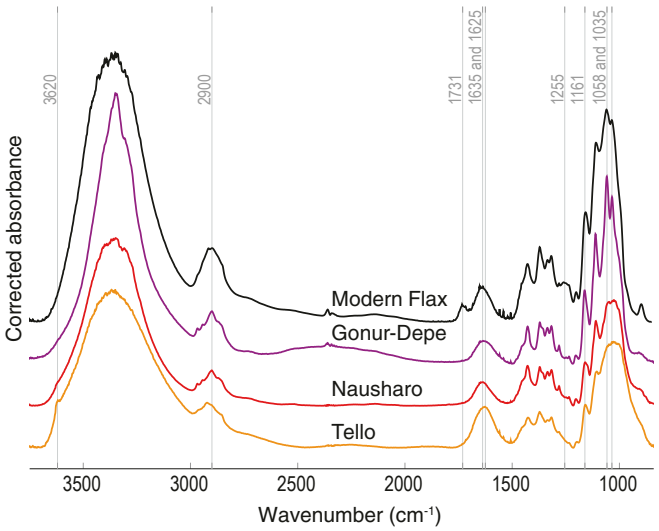

Fig. 2. Fourier-transform infrared absorbance spectra of archaeological textile and reference samples. The IR signature of cellulose is visible in all archaeological spectra. The spectra were corrected for sample thickness to allow a semiquantitative comparison of the intensity of the absorption bands (47). Note the disappearance of the absorption band at 1,731 cm^{-1}; the apparition of a shoulder at 3,620 cm^{-1} in the spectra of archaeological samples; and the decrease in intensity with increasing mineralization of the absorption bands centered at 2,900, 1,161, 1,058, and 1,035 cm^{-1}.

To study the fibers at very high spatial resolution by μ-FTIR overcoming the spatial resolution limit (typically 5 μm) due to diffraction, we have developed a protocol based on atomic force microscopy–infrared (AFM-IR) nanospectroscopy (Fig 3 *A* and *B* and *SI Appendix*, Text S1) (26). We observed a significant gradient in the alteration of cellulose from the surface to the lumen in a cross-section of a fiber from Nausharo (Fig. 3*D*). The intensity of the absorption bands at 1,107 and 1,058 cm^{-1}, characteristic of the secondary and primary alcohols of cellulose, respectively (elongation modes of the C–O bond; *SI Appendix*, Table S4), increases significantly from the fiber surface to the lumen. This suggests that the diffusion of solutes from the soil and from corrosion of metal objects through the cell walls plays a critical role in the degradation of organic macromolecules.

Crystallinity and Fluid Transport

Positive mineralization of cellulosic fibers involves aqueous transport of inorganic compounds through all their cell walls, a process that strongly depends on the local crystallinity of the latter (28). Plant fibers have a relatively high degree of crystallinity for polymeric systems (65 to 70%) owing to the multiscale mesostructuration of cellulose (semicrystalline polysaccharide) (29). Within the cell walls, the cellulosic macromolecular chains are packed into microfibrils (10 to 30 nm in diameter), themselves aggregated into macrofibrils (typically 1 μm in diameter). The Iβ form of cellulose crystalline domains, primarily present in plant fibers, crystallizes in a monoclinic system and a $P2_1$ space group (30). These domains are therefore noncentrosymmetric and have a nonnull second-order nonlinear susceptibility, $\chi^{(2)}$, leading to second harmonic generation (SHG) under suitable experimental conditions (31). Hemicellulose and lignin molecules, which provide mechanical and chemical resistance

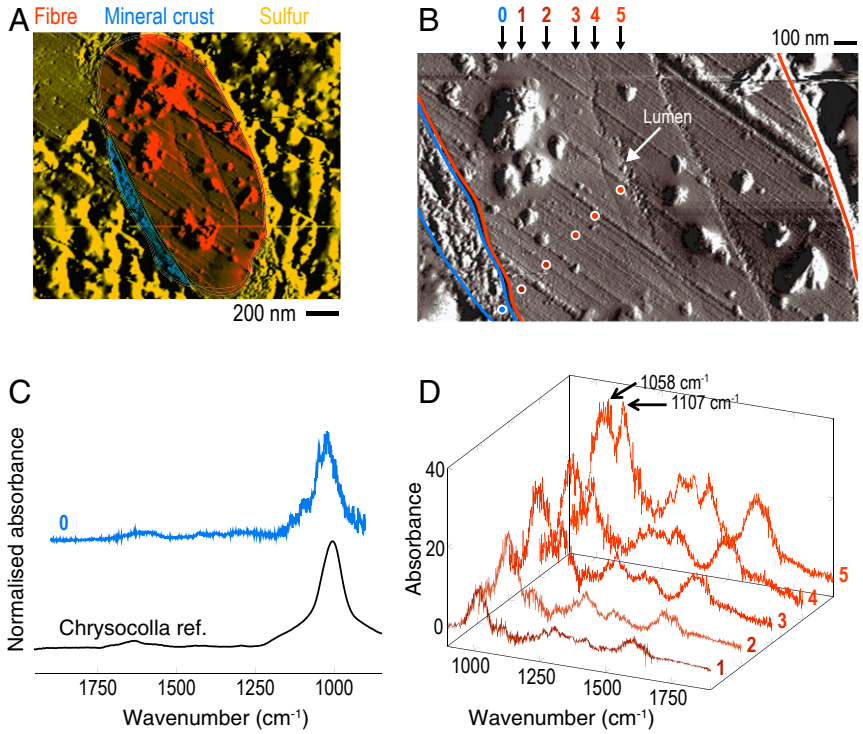

Fig. 3. Nanoresolved identification of chemical species across the cross-section of a fiber from the Nausharo site. (*A*) Deflection image obtained by atomic force microscopy of the cross-section of a fiber of the Nausharo site, using sulfur as the embedding medium. (*B*) Close-up of the cross-section. The dots identify spots of interest: one located on the mineral phase (0) and five on a line from the surface toward the lumen of the fiber (1 to 5). (*C*) Normalized AFM-IR spectrum collected in spot 0 (top) and normalized FTIR spectrum of chrysocolla (bottom) (27). (*D*) Raw AFM-IR spectra collected in spots 1 to 5 (48). The wavenumber axis is inverted with respect to *C* for better readability.

to plant fibers by cross-linking cellulose micro- and macrofibrils, are centrosymmetric (amorphous) polymers that do not contribute to the SHG signal. SHG microscopy therefore provides specific imaging of the crystalline cellulosic domains in cellulosic materials (32). One fiber from each archaeological sample was analyzed in SHG under strictly identical analytical conditions (*SI Appendix*, Text S1). The images appear particularly contrasted and detailed and show a lesser degree of

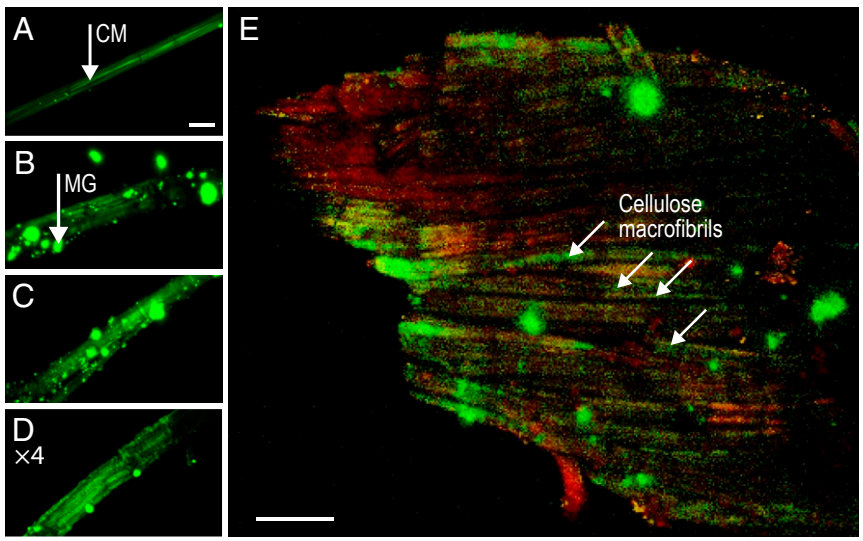

Fig. 4. Visualization of cellulose macrofibrils in the archaeological fibers using second harmonic generation microscopy. (*A–D*) SHG microscopy images of the fibers in their median plane (pixel size: 420 × 420 nm^2): modern flax (*A*), Gonur-Depe (*B*), Nausharo (*C*), and Tello (*D*) (49). The four samples were analyzed under strictly identical conditions to allow intercomparison of the images (see *SI Appendix*, Text S1 for details). The intensity of *D* was multiplied by a factor of 4 as it is far weaker than the three others. CM, cellulose microfibril; MG, noncentrosymmetric mineral grain. (Scale bar for *A–D*: 20 μm.) (*E*) Backward SHG microscopy reconstructed in-focus image of a bundle of fibers collected directly on the textile from Tello. The fluorescence and SHG signals are shown in red and green, respectively. (Scale bar: 50 μm.)

disorganization in the less-mineralized fibers (Fig. 4*A*). Yet, even in the most altered fibers of Tello, we observed some macrofibrils of 1 to 2 μm in diameter, in the form of short fragments, as a consequence of macromolecular degradation (Fig. 4*B* and *SI Appendix*, Fig. S12*C*). Remnant macrofibrils in all samples are clearly oriented along the fiber axis as in native fibers (33, 34): this is quantitatively shown by the polarization curve of the Gonur-Depe sample, which is well fitted by a type I phase model (*SI Appendix*, Fig. S12 *A*, *C*, and *D*). The fiber from the Gonur-Depe site, whose organic phase appears extremely well preserved, generates a SHG signal comparable to that found in modern flax.

Insight into the Mineralization Mechanisms

These results provide an unprecedented insight into the mechanisms that led to the exceptional preservation of the cellulosic material at a nanoscale. A consistent pattern emerges comprising three steps (Fig. 5):

Step 1: Water Transport of Biocidal Metal Cations and Soil Solutes. While plant fibers are normally degraded within a few weeks after burial in soil (35) by microorganism enzymes such as cellulases and cellobiose dehydrogenase, which catalyze the hydrolysis and oxidation of cellulose, respectively, we consistently observed the presence of cellulosic signatures in all three archaeological samples (FTIR). This is attributed to the inhibition of enzyme production and enzymatic reactions by metal cations released during the corrosion of metal objects buried in the vicinity of the textiles, in this case copper based (16). The formation of reactive oxygen species such as hydroxyl radicals ($M^{n+} + H_2O_2 \rightleftarrows M^{(n+1)+} + HO^{\cdot} + HO^{-}$, where M denotes the metal cation) induces oxidative stress in microorganisms and fungi, thereby inhibiting their enzymatic production. Short-term protection of fibers is an essential step to allow time for slower chemical reactions to occur before molecular degradation. The fibers from the Gonur-Depe site come from a fabric enveloping a copper "ladder" in several layers in a funerary context (*SI Appendix*, Text S1). The compactness of this medium probably contributed to limiting very strongly the percolation of water from the environment and the impregnation of the fibers; they are made of an exceptionally preserved organic matrix surrounded by a discontinuous inorganic crust of mineral grains (Fig. 1).

Step 2: Degradation and Loss of Crystallinity of Cellulosic Polysaccharides. The most easily accessible, amorphous, areas of the cellulosic material hydrolyzed first as evidenced by the systematic absence of signals from hemicelluloses (FTIR). Even the least-degraded fibers, from the Gonur-Depe site, contain no or highly hydrolyzed hemicelluloses, while their cellulose content appears only slightly chemically degraded with quasi-intact molecular packing at the mesoscale (SHG). The successive steps of diffusion through the cell walls, adsorption and hydrolysis by water, a good solvent (36) for cellulose (interactions between polymer chains and water molecules are energetically favorable), explain the irreversible swelling of the fibers (37). The lumen of archaeological fibers sometimes appears up to 20 times wider than that of modern flax, which we attribute to this swelling in addition to the original size dispersal. Indeed, the larger fibers from the Gonur-Depe and Tello sites show the formation of microcracks from their lumen, which are likely the result of swelling of the polymer network (Fig. 1*B*) (38). The accumulation of solutes on the surface of the fibers in interaction with hydroxyl groups from superficial cellulosic chains (weak interactions, complexation, or condensation with cupric ions Cu^{2+} and silicate compounds $H_4SiO_4^0$, $H_3SiO_4^-$, etc.) led to the precipitation of the inorganic crust (39, 40). This crust, present on the surface of the Gonur-Depe and Nausharo fibers, constituted a mineral reservoir and a barrier which must have considerably limited the degradation of the fibers by insects, fungi, and microorganisms (35). The subsequent diffusion of mineral-rich fluids, which may explain the greater preservation of cellulosic residues closer to the fiber lumens, is typical of a diffusion profile. This process

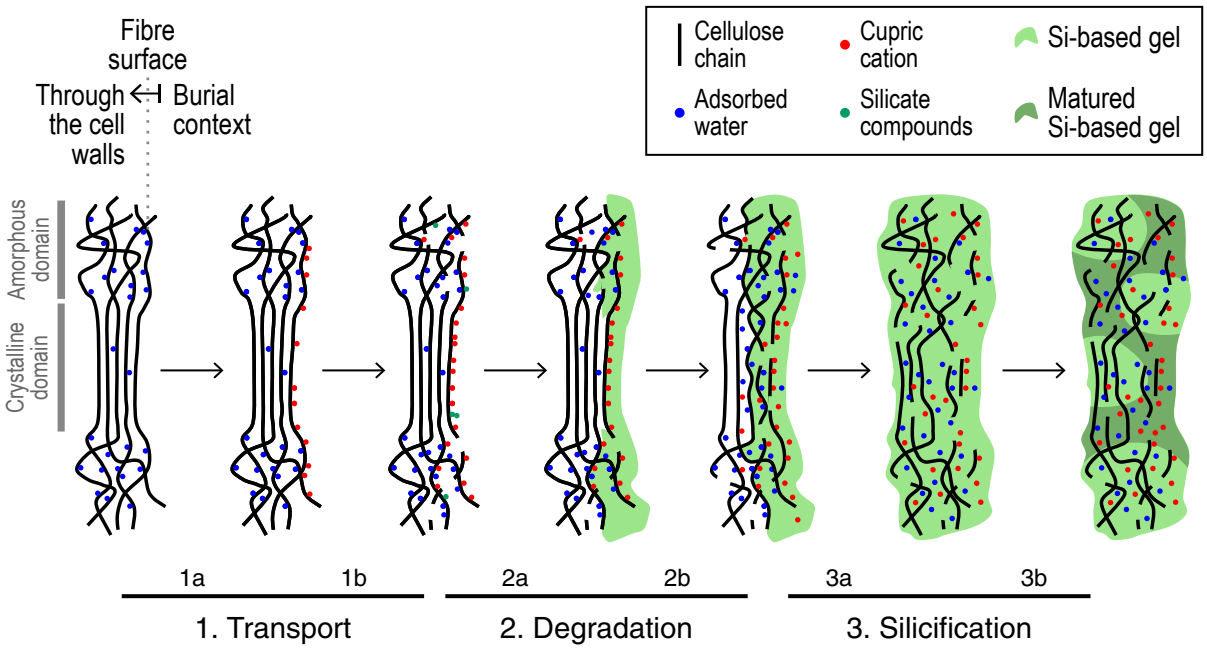

Fig. 5. Mechanism for cellulosic fiber mineralization over time. Step 1: Water transport of biocidal metal cations and soil solutes—formation of copper–cellulose complexes at the surface of the fibers (1a) and hydrolysis of amorphous compounds and condensation of silicates on fiber surface and in amorphous areas (1b). Step 2: Degradation and loss of crystallinity of cellulosic polysaccharides—degradation of the superficial macromolecules of the crystalline zones (2a) and local swelling (2b). Step 3: Silicification—diffusion of solutes deeper into the cell walls and condensation of siliceous compounds (3a) and maturation in denser siliceous phases (3b).

results in the formation of an intermediate attenuation phase present on the surface of the Gonur-Depe fiber (120 cm^{-1}), while it is present in the cell walls of the Nausharo fibers, indicating the gradual transport of metal cations and soil solutes from the inorganic crust to the fiber lumen over time (Fig. 1 *C* and *D*). The inorganic crust of the two samples also contains the unknown phases of attenuation coefficients 180 and 250 cm^{-1} (Fig. 1 *C* and *D*), which could not be ascribed to any common corrosion products (*SI Appendix*, Table S1). The μ-FTIR spectra collected from the samples from Gonur-Depe and Nausharo show a shoulder at 3,620 cm^{-1} (Fig. 2). An intense absorption at 1,020 cm^{-1} is detected by AFM-IR spectroscopy on the mineral crust of the Nausharo sample (Fig. 3*C*, spot 0). Both features are respectively characteristic of elongation modes of O–H and of Si–O bonds in silicates and hydroxysilicates with spectral features very similar to that of chrysocolla (Fig. 3*C* and *SI Appendix*, Fig. S10). In fact, attenuation of 180 to 350 cm^{-1} is typical of copper silicates (*SI Appendix*, Table S3). No diffraction signals could be observed from the analysis of a cross-section comprising a few fibers from the Nausharo sample by electron backscatter diffraction (EBSD) or from analysis by X-ray diffraction on the Nausharo and Tello samples. This confirms the amorphous nature of these silicate phases.

Step 3: Silicification. In the longer term, the degradation of cellulose in the cell walls has led to increased disorganization of the crystalline domains, allowing the diffusion of solutes at greater depth. The sustained presence of copper cations, as essential precursors for the formation of reactive oxygen species, may have facilitated the degradation of cellulosic fibers (41). Interestingly, none of the oxidized copper compounds that are common in archaeological samples, such as $CuCl_{(s)}$, $CuCl_{2(s)}$, $Cu_2O_{(s)}$, or $Cu_2CO_3(OH)_{2(s)}$, were identified in the cell walls of the fibers. The cell walls of the most-mineralized fibers from Tello are completely filled by the three highly attenuating phases at ca. 180, 250, and 350 cm^{-1}, the latter also being attributable to a denser phase of copper silicates (μ-CT; *SI Appendix*, Table S3). The phase of intermediate attenuation (120 cm^{-1}) observed in the Gonur-Depe and Nausharo samples is absent. We therefore evidence at nanoscale that the denser copper silicate phase most probably results from a maturation process of the lighter phase, as in silicified wood where opal-A is gradually transformed into opal-CT and then quartz over time (42, 43). More limited percolation in fine-grained sandy sediments, and therefore limited solubilization of silicon, may explain why lignocellulose appears to be better preserved in coarse-grained sediments (7).

Conclusion

Our results therefore provide unique insights at the nanoscale on the mineralization of cellulosic fibers over 4,000 to 5,000 years. The dual role of metal cations as protection against microorganisms and precursor of a slow degradation of polysaccharides allowing percolation of water at greater depth in fibers appears essential (17, 19). We have documented the complex interplay between the three steps of protection, controlled alteration, and silicification. The unprecedented demonstration of the preservation of cellulose in place, at the macrofibril level, after 5,000 years, further consolidates the interest of the concept of "pockets of preservation" (44, 45) and shows promise for future single-molecule studies of plant fossils. This study highlights the contribution of spectral imaging techniques to decipher the fundamental processes underlying fossilization at the nanoscale. SHG microscopy is demonstrated to be a particularly powerful method to investigate the molecular organization in fossil systems at a three-dimensional (3D) submicroscale.

Materials and Methods

Materials. Mineralized cellulosic fibers from three excavation sites were studied, with varying degrees of alteration (*SI Appendix*, Fig. S1). Details on the excavations, the archaeological and geological contexts, and the appearance of the samples are given in *SI Appendix*, Text S1. The best-preserved textile sample was collected from the Gonur-Depe site (present-day Turkmenistan). The soft brownish fabric dates from the second millennium BCE. This sample was extracted in 2001 from the grave of a warrior. It was found buried next to several copper-based objects, including a ladder, a short sword, and a cup. The sample from the Nausharo site (Baluchistan, present-day Pakistan) is dated to the third millennium BCE. The sample, a corroded copper plate with textile remains on the surface, was collected in 1995. Its threads are made of brown and brittle fibers. The textile from the Tello site (present-day Iraq) is dated to the second millennium BCE. Textile remains on a copper-base belly vase were excavated between 1929 and 1931. The fragment studied is a braided fabric weaved in a simple plain tabby, with S-twist yarns. The blue-green fibers it is made of are very friable and appear highly mineralized. This fragment belongs to the Département des Antiquités Orientales at Musée du Louvre. Although at different stages of chemical transformation, this corpus was constructed to present similarities in age, soil context, and material type (cellulosic tissue, all identified as probably flax, and association with a copper substrate). A sample of modern flax was additionally studied as a reference (Haute-Normandie, France).

Synchrotron X-Ray Microtomography. Synchrotron X-ray microtomography was carried out at the ANATOMIX (Advanced Nanotomography and Imaging with coherent X-rays) beamline of the SOLEIL synchrotron. The isolated yarns and fibers were fixed vertically to a support using glue (*SI Appendix*, Fig. S2) to ensure their immobility during the rotation of the stage. A synchrotron monochromatic X-ray beam of 10 keV was obtained using a Si(111) double-crystal monochromator and focused using beryllium compound refractive lenses. The on-sample photon flux is estimated at 5×10^{11} photon·mm^{-2} · s^{-1}. The transmitted X-rays were converted into visible light using a LuAG:Ce (lutetium aluminum garnet) scintillator and transferred to the lens (20×, numerical aperture [NA] = 0.42) of the camera (ORCA-Flash4.0 V2; Hamamatsu Photonics; 2,048 × 2,048 pixels of 6.5 μm lateral size). For each sample, 2,000 radiographs were acquired on 180° to generate a tomogram (200 ms per radiograph). The local value of the linear attenuation coefficient $\mu_E(X)$ for each voxel X in the sample was reconstructed using the PyHST software. The resulting voxel lateral size is 325 nm. The obtained reconstructed images were further processed using the ImageJ software (*SI Appendix*, Text S2).

μ-FTIR Spectroscopy. μ-FTIR spectroscopy was collected using the Vortex 70 spectrometer coupled to an HYPERION 3000 microscope at IPANEMA. A fiber was carefully extracted from each sample, flattened with a diamond cell, and transferred to a calcium fluoride ($CaF_{2\,(s)}$) substrate. Spectra were collected in transmission using a $N_{2(l)}$-cooled MCT detector (mercury cadmium telluride HgCdTe, energy domain 4,000 to 800 cm^{-1}, 128 scans; energy resolution 4 cm^{-1}). The window defining the area analyzed was chosen to avoid collecting outside the sample. The IR spectra were corrected from a background spectrum collected under identical conditions. A correction was implemented to correct the absorbance from the thickness, e_r, of the flattened fiber. e_r was measured using the AFM at the SMIS beamline of the SOLEIL synchrotron, by measuring the difference in height between the flattened fiber surface and the substrate (*SI Appendix*, Text S1).

AFM-IR Spectroscopy. Sample preparation was carried out in the clean room of the Centre de Sciences Nucléaires et de Sciences de la Matière (CSNSM) (*SI Appendix*, Fig. S3). A specific methodology was implemented to overcome the impossibility of preparing thin sections (500 nm and 1 μm thick) by conventional means. Solid sulfur (99.98%; Sigma Aldrich) was liquefied at 115 °C on a hot plate. One fiber per series was immersed in a supercooling sulfur drop under binoculars. Once crystallized, the sulfur drops were moved on ultramicrotomy supports and flattened using a diamond knife to obtain a surface flat enough to be analyzed by AFM. The flattened drops were transferred to a metal support using a watchmaker's saw. Measurements were carried out using the AFM-IR instrument (nanoIR2-FS; Bruker Anasys Instruments) at Institut de Chimie Physique. The spectra were collected in contact mode using a gold-coated AFM tip, with illumination from above to increase the signal generated by the lightning-rod effect. Four complementary energy-range IR sources were used (global spectral range 1,900 cm to 900 cm^{-1}). The raw data were processed using the Analysis Studio software,

using the Spectral Discontinuity tool to correct the effect of using all four sources (*SI Appendix*, Text S1).

Second Harmonic Generation Microscopy. SHG microscopy was performed at the Laboratoire d'Optique et Biosciences (LOB) (École Polytechnique, Palaiseau, France). The fibers were placed on a concave microscope slide covered with a protective glass slide (*SI Appendix*, Fig. S4). The monochromatic beam of a titanium–sapphire laser (λ = 860 nm) was focused on the sample via a water-immersion 25×, NA = 1.05 objective or an air 5×, NA = 0.5 objective. Under the objective, the power at the sample surface is between 9 and 24 mW. The anisotropically emitted SHG signal (at $\lambda/2$ = 430 nm) was collected "forward" and "backward." The isotropically emitted fluorescence signal was collected backward. Raster-scanned images were collected using a motorized optical system in the (*x*0*y*) plane and at different depths *z* through the samples (lateral pixel size of 0.43 or 0.85 μm depending on acquisition). The image in Fig. 4*E* was corrected to be in focus over the entire thickness of the specimen using the 3D viewer plugin of the ImageJ software. The polarization state on the sample surface is controlled by a pair of achromatic quarter and half waveplates to switch from linear to circular polarizations and to control the orientation of linear polarization (*SI Appendix*, Text S4).

Additional information on materials and methods is available in *SI Appendix*, Text S1.

ACKNOWLEDGMENTS. We thank Maëva L'Héronde, Guillaume Le Bourdellès (IPANEMA), and Cécile Engrand (Centre de Sciences Nucléaires et de Sciences de la Matière, Orsay, France) for their support in sample preparation and data acquisition. We thank Timm Weitkamp for his interest, advice, and support at the ANATOMIX beamline. ANATOMIX is an Equipment of Excellence funded by the "Investments for the Future" program of the French National Research Agency (Agence Nationale de la Recherche [ANR]), project NanoimagesX, Grant ANR-11-EQPX-0031. We thank Marie-Claire Schanne-Klein for fruitful discussions and ANR for funding support (Contracts ANR-11-EQPX-0029 Morphoscope2 and ANR-10-INBS-04 France). Complementary characterization in EBSD was performed by Cécile Fossé (IPANEMA) and Luc Robbiola (TRACES [Travaux de recherches archéologiques sur les cultures, les espaces et les sociétés], UMR 5608, Toulouse, France). We thank colleagues at the SMIS beamline of SOLEIL for access to the AFM at the beamline. The work of J.L. was supported by the LabEx (Laboratoire d'Excellence) PATRIMA/Fondation des Sciences du Patrimoine under Project ETAM++. L.B. and M.T. acknowledge support from the Research Infrastructures activity IPERION CH (Integrated Platform for the European Research Infrastructure ON Cultural Heritage) of the Horizon2020 Program of the European Union (Grant 654028). Nanoinfrared imaging was carried out using a microscope supported by the NIRMA (Nano-imagerie InfraRouge pour les Matériaux Anciens) project of the Région Île-de-France/DIM (Domaine d'intérêt majeur) Matériaux Anciens et Patrimoniaux.

1. J. L. Townson *et al.*, Synthetic fossilization of soft biological tissues and their shape-preserving transformation into silica or electron-conductive replicas. *Nat. Commun.* **5**, 5665 (2014).
2. A. Kish *et al.*, Preservation of archaeal surface layer structure during mineralization. *Sci. Rep.* **6**, 26152 (2016).
3. D. E. Briggs, A. J. Kear, Fossilization of soft tissue in the laboratory. *Science* **259**, 1439–1442 (1993).
4. U. Bergmann, P. L. Manning, R. A. Wogelius, Chemical mapping of paleontological and archeological artifacts with synchrotron X-rays. *Ann. Rev. Anal. Chem.* **5**, 361–389 (2012).
5. Y. C. Lee *et al.*, Evidence of preserved collagen in an Early Jurassic sauropodomorph dinosaur revealed by synchrotron FTIR microspectroscopy. *Nat. Comm.* **8**, 14220 (2017).
6. J. Alleon *et al.*, Chemical nature of the 3.4 Ga Strelley Pool microfossils. *Geochem. Persp. Lett.* **7**, 37–42 (2018).
7. D. E. Briggs, R. P. Evershed, M. J. Lockheart, The biomolecular paleontology of continental fossils. *Paleobiology* **26** (suppl. 4), 169–193 (2000).
8. E. R. Locatelli, "The exceptional preservation of plant fossils: A review of taphonomic pathways and biases in the fossil record" in *Reading and Writing of the Fossil Record: Preservational Pathways to Exceptional Fossilization, The Paleontological Society Papers*, M. Laflamme, J. D. Schiffbauer, S. A. F. Darroch, Eds. (Cambridge University Press, 2014), vol. 20, pp. 237–258.
9. M. Liesegang, C. T. Gee, Silica entry and accumulation in standing trees in a hot-spring environment: Cellular pathways, rapid pace and fossilization potential. *Palaeontology* **63**, 1–10 (2020).
10. M. E. Collinson, "Molecular taphonomy of plant organic skeletons" in *Taphonomy in Process and Bias through Time*, P. A. Allison, D. J. Bottjer, Eds. (Springer, Dordrecht, The Netherlands, ed. 2, 2011), vol. 32, pp. 223–248.
11. K. Arshad, M. Skrifvars, V. Vivod, J. Valh, B. Voncina, Biodegradation of natural textile materials in soil. *Tekstilec* **57**, 118–132 (2014).
12. G. Mustoe, Wood petrifaction: A new view of permineralization and replacement. *Geosciences* **7**, 119 (2017).
13. R. D. Gillard, S. M. Hardman, R. G. Thomas, D. E. Watkinson, The mineralization of fibres in burial environments. *Stud. Conserv.* **39**, 132–140 (1994).
14. L. Biek, *Archaeology and the Microscope: The Scientific Examination of Archaeological Evidence* (Lutterworth Press, London, UK, 1965).
15. J. E. Vollmer, "Textile pseudomorphs on Chinese bronzes" in *Proceedings, Irene Emery Roundtable on Museum Textiles, 1974, Washington, DC*, P. L. Fiske, Ed. (The Textile Museum, Washington, DC, 1975), pp. 170–174.
16. L. Bertrand, A. Vichi, J. Doucet, P. Walter, P. Blanchard, The fate of archaeological keratin fibers in a temperate burial context: Microtaphonomy study of hairs from Marie de Bretagne (15th c., Orléans, France). *J. Archaeol. Sci.* **42**, 487–499 (2014).
17. H. Chen, K. Jakes, D. Foreman, Preservation of archaeological textiles through fibre mineralization. *J. Archaeol. Sci.* **25**, 1015–1021 (1998).
18. I. Good, Archaeological textiles: A review of current research. *Annu. Rev. Anthropol.* **30**, 209–226 (2001).
19. C. Moulhérat, Archéologie des textiles. Une nouvelle méthodologie appliquée à l'étude des tissus minéralisés. *Nouvelles de l'Archéologie* **114**, 18–23 (2008).
20. D. E. G. Briggs, The role of decay and mineralization in the preservation of soft-bodied fossils. *Annu. Rev. Earth Planet. Sci.* **31**, 275–301 (2003).
21. T. Weitkamp *et al.*, The tomography beamline ANATOMIX at Synchrotron SOLEIL. *J. Phys. Conf.* **849**, 012037 (2017).
22. M. Smole, S. Hribernik, K. Stana-Kleinschek, T. Kerze, "Plant fibres for textile and technical applications" in *Advances in Agrophysical Research*, S. Grundas, A. Stepniewski, Eds. (IntechOpen, London, UK, 2013), pp. 369–398.
23. A. Jacobs, M. Palm, G. Zacchi, O. Dahkman, Isolation and characterization of water-soluble hemicelluloses from flax shive. *Carbohydr. Res.* **338**, 1869–1876 (2003).
24. A. Shrotri, L. K. Lambert, A. Tanksale, J. Beltramini, Mechanical depolymerisation of acidulated cellulose: Understanding the solubility of high molecular weight oligomers. *Green Chem.* **15**, 2761–2768 (2013).
25. O. Haske-Cornelius *et al.*, Environmentally friendly covalent coupling of proteins onto oxidized cellulosic materials. *New J. Chem.* **43**, 14536–14545 (2019).
26. A. Dazzi, C. B. Prater, AFM-IR: Technology and applications in nanoscale infrared spectroscopy and chemical imaging. *Chem. Rev.* **117**, 5146–5173 (2016).
27. B. Lafuente, R. T. Downs, H. Yang, N. Stone, Data from "Chrysocolla R050053.1." RRUFF. https://rruff.info/Chrysocolla/R050053. Accessed 3 March 2020.
28. A. Mihranyan, A. Piñas Llagostera, R. Karmhag, M. Strømme, R. Ek, Moisture sorption by cellulose powders of varying crystallinity. *Int. J. Pharm.* **269**, 433–442 (2004).
29. A. C. O'Sullivan, Cellulose: The structure slowly unravels. *Cellulose* **4**, 173–207 (1997).
30. Y. Nishiyama, P. Langan, H. Chanzy, Crystal structure and hydrogen-bonding system in cellulose Iβ from synchrotron X-ray and neutron fiber diffraction. *J. Am. Chem. Soc.* **124**, 9074–9082 (2002).
31. R. M. Brown, A. C. Millard, P. J. Campagnola, Macromolecular structure of cellulose studied by second-harmonic generation imaging microscopy. *Optic Lett.* **28**, 2207–2209 (2003).
32. G. Latour, J.-P. Echard, M. Didier, M.-C. Schanne-Klein, In situ 3D characterization of historical coatings and wood using multimodal nonlinear optical microscopy. *Opt. Express* **20**, 24623–24635 (2012).
33. A. Peterlin, P. Ingram, Morphology of secondary wall fibrils in cotton. *Textil. Res. J.* **40**, 345–354 (1970).
34. C. Bergfjord *et al.*, Comment on "30,000-year-old wild flax fibers". *Science* **328**, 1634 (2010).
35. R. López-Mondéjar, D. Zühlke, D. Becher, K. Riedel, P. Baldrian, Cellulose and hemicellulose decomposition by forest soil bacteria proceeds by the action of structurally variable enzymatic systems. *Sci. Rep.* **6**, 25279 (2016).
36. S. Koltzenburg, M. Maskos, O. Nuyken, "Polymers in solution" in *Polymer Chemistry* (Springer, Berlin/Heidelberg, Germany, 2017), pp. 17–37.
37. C. Mingyang, B. Coasne, R. Guyer, D. Derome, J. Carmeliet, Role of hydrogen bonding in hysteresis observed in sorption-induced swelling of soft nanoporous poymers. *Nat. Commun.* **9**, 3507 (2018).
38. G. W. Miller, S. A. D. Visser, A. S. Morecroft, On the solvent stress-cracking of polycarbonate. *Polym. Eng. Sci.* **11**, 73–82 (1971).
39. R. Michie, Sorption of copper by cellulose. *Nature* **190**, 803–804 (1961).
40. J. Huang, T. Kunitake, Nano-precision replication of natural cellulosic substances by metal oxides. *J. Am. Chem. Soc.* **125**, 11834–11835 (2003).
41. J. C. Williams, C. S. Fowler, M. S. Lyon, T. L. Merrill, Metallic catalysts in the oxidative degradation of paper. *Adv. Chem.* **164**, 37–61 (1978).
42. R. F. Leo, E. S. Barghoorn, "Silicification of wood" in *Botanical Museum Leaflets* (Harvard University, 1976), vol. 25, pp. 1–47.
43. R. Hesse, Silica diagenesis: Origin of inorganic and replacement cherts. *Earth Sci. Rev.* **26**, 253–284 (1989).
44. J. Anné *et al.*, Advances in bone preservation: Identifying possible collagen preservation using sulfur speciation mapping. *Palaeogeogr. Palaeoclimatol. Palaeoecol.* **520**, 181–187 (2019).
45. R. Georgiou *et al.*, Carbon speciation in organic fossils using 2D to 3D x-ray Raman multispectral imaging. *Sci. Adv.* **5**, eaaw5019 (2019).
46. C. Reynaud *et al.*, Tomography. Zenodo. https://doi.org/10.5281/zenodo.3712368. Deposited 15 July 2020.
47. C. Reynaud *et al.*, FTIR. Zenodo. https://doi.org/10.5281/zenodo.3712368. Deposited 15 July 2020.
48. C. Reynaud *et al.*, AFM-IR. Zenodo. https://doi.org/10.5281/zenodo.3712368. Deposited 15 July 2020.
49. C. Reynaud *et al.*, SHG. Zenodo. https://doi.org/10.5281/zenodo.3712368. Deposited 15 July 2020.